Journal of the Meteorological Society of Japan, **99**(1), 5−25, 2021. doi:10.2151/jmsj.2021-001
Special Edition on Global Precipitation Measurement (GPM): 5th Anniversary

Large Precipitation Gradients along the South Coast of Alaska Revealed by Spaceborne Radars

Shunsuke AOKI and Shoichi SHIGE

Graduate School of Science, Kyoto University, Kyoto, Japan

(Manuscript received 18 February 2020, in final form 15 September 2020)

Abstract

This study focuses on the considerable spatial variability of precipitation along the western coast of a continent at mid–high latitude and investigates the precipitation climatology and mechanism along the south coast of Alaska, using datasets of spaceborne radars onboard two satellites, namely, the Dual-frequency Precipitation Radar (DPR) KuPR onboard the Global Precipitation Measurement (GPM) core satellite and the Cloud Profiling Radar (CPR) onboard CloudSat. At higher latitudes, differentiating the phase of precipitation particles falling on the ground is crucial in evaluating precipitation. Classification of satellite precipitation products according to the distance from the coastline shows that precipitation characteristics differ greatly on opposite sides of the coastline. Above coastal waters, relatively heavy precipitation with CPR reflectivity larger than 7 dBZ from orographically enhanced nimbostratus clouds, which can be detected by KuPR, is frequently captured. Meanwhile, along coastal mountains, light-to-moderate snowfall events with CPR reflectivity lower than 11 dBZ, which are well detected by the CPR but rarely detected by KuPR, frequently occur, and they are mainly brought by nimbostratus clouds advected from the coast and orographically enhanced shallow cumuliform clouds. There is no clear diurnal variation of precipitation except in summer, and the amplitude of the variation during summer is still low compared with total precipitation especially over the ocean, suggesting that the transport of synoptic-scale water vapor brings much precipitation throughout the year. Case studies and seasonal analysis indicate that frontal systems and moisture flows associated with extratropical cyclones that arrive from the Gulf of Alaska are blocked by terrain and stagnate along the coast to yield long-lasting precipitation along the coastline. The results of this study illustrate the importance of using complementary information provided by these radars to evaluate the precipitation climatology in a region in which both rainfall and snowfall occur.

Keywords orographic precipitation; hydrological cycle; spaceborne radar

Citation Aoki, S., and S. Shige, 2021: Large precipitation gradients along the south coast of Alaska revealed by spaceborne radars. *J. Meteor. Soc. Japan*, **99**, 5–25, doi:10.2151/jmsj.2021-001.

1. Introduction

Coastal areas receive a large amount of precipitation owing to their vicinity to the source of moisture. It has been revealed that, within tropical areas, the concentration of precipitation in coastal regions due to the diurnally driven precipitation system and orographically enhanced moist monsoon flow plays an important role in the global circulation of water between ocean and land (Ogino et al. 2017). Although precipitation declines toward polar regions owing to the low water-carrying capacity of the atmosphere, precipitation at higher latitude still has important scientific and social meaning. In the extratropics, especially along the western coasts of continents, the forced ascent of moist air in synoptic weather systems

Corresponding author: Shunsuke Aoki, Division of Earth and Planetary Sciences, Graduate School of Science, Kyoto University, Kitashirakawa-oiwake, Sakyo, Kyoto 606-8502, Japan
E-mail: aoki.shunsuke@kugi.kyoto-u.ac.jp
J-stage Advance Published Date: 21 October 2020

and prevailing westerly flow over mountain ranges cause heavy precipitation, frequently causing disastrous flooding and landslides (Medina et al. 2007; Houze 2012; Zagrodnik et al. 2018). Because the temperature is close to the melting point of water owing to the higher altitude and latitude, what characterizes the precipitation climatology along the coastlines is not only the amount of precipitation but also the phase of precipitation particles falling to the surface, which is not much of an issue when referring to tropical precipitation. Snowfall at high latitudes and in mountain regions at midlatitudes maintains the mass of glaciers and icefields that play the important role of great freshwater reservoirs, whereas rainfall in these regions increases the flow of rivers to the sea and the melting of ice. It is thus important to reveal both the amount and phase of precipitation in grasping the global hydrological cycle.

A satellite-based precipitation dataset is useful in grasping the characteristics of precipitation in a region having sparse and biased ground-based observations due to the complicated orography and inaccessibility of the region. In particular, spaceborne radars have an advantage in observing such regions in that they can capture the vertical structure of precipitation regardless of the surface condition. Furthermore, the high horizontal resolution allows the delineation of spatial gradients of precipitation at scales of crests and valleys over several tens of kilometers in mountainous areas. As an example, the 17-year observations of the Tropical Rainfall Measuring Mission (TRMM; Kummerow et al. 1998) Precipitation Radar (PR; Kozu et al. 2001) have provided much insight into the precipitation process along tropical coastlines (Mori et al. 2004; Ogino et al. 2016) and orographic effects on precipitating clouds (Nesbitt and Anders 2009; Shige and Kummerow 2016; Shige et al. 2017; Hirose et al. 2017); these have been difficult to capture using passive infrared or microwave imagers onboard satellites (Biasutti et al. 2012; Houze 2012).

Currently, there are two spaceborne platforms in orbit with radars capable of measuring precipitation: the Global Precipitation Measurement (GPM) mission Core Observatory (Hou et al. 2014) and CloudSat (Stephens et al. 2002). The Dual-frequency Precipitation Radar (DPR) onboard GPM Core, which was launched in 2014, has Ku-band (13.6-GHz) and Ka-band (35.55-GHz) radars designed to measure rainfall and snowfall (Kojima et al. 2012; Iguchi 2020). GPM DPR products cover a mid–high latitudinal area, which the TRMM PR product does not cover, owing to the higher-angled non-sun-synchronous orbit (approximately 65° for GPM versus 35° for TRMM) of GPM Core. CloudSat has carried the W-band (94-GHz) Cloud Profiling Radar (CPR; Tanelli et al. 2008) in near-polar sun-synchronous orbit since its launch in 2006. Although the CPR was primarily designed to observe clouds, it can also detect precipitation. Many studies have compared the CPR and DPR in terms of global precipitation measurements (Casella et al. 2017; Tang et al. 2017; Skofronick-Jackson et al. 2019) and found that the CPR is far more sensitive in measuring light-to-moderate rainfall and snowfall than the DPR due to the CPR's higher sensitivity and finer horizontal resolution (approximately 1 km for the CPR versus approximately 5 km for the DPR). Although suffering from low detectability, the DPR has a good sampling rate owing to its scanning in the cross-track direction. Furthermore, the DPR can measure the intensity of modest-to-heavy precipitation, whereas the CPR cannot owing to its large attenuation and multiple-scattering effect (Berg et al. 2010; Chen et al. 2016; Tang et al. 2017; Skofronick-Jackson et al. 2019). It is effective to use complementary information provided by these radars in evaluating precipitation features in a region in which both rain and snow fall.

Among coastal areas at higher latitude, the south coast of Alaska (45–65°N, 125–155°W) is selected for analysis in this study because precipitation concentrates along this coast over a long narrow area of > 1000 km. Precipitation along the west coast of North America is usually associated with extratropical cyclones arriving from the Pacific Ocean (Medina et al. 2007), which may be the same for other western continental mountain regions, such as the mountain regions of Patagonia, Norway, and New Zealand. Terrain sometimes blocks low-level air flow so that it produces a strong terrain-parallel component of wind, which is called a barrier jet, and modifies the near upstream moisture flow and rain rate. Low-level air flow is sometimes lifted by orography and enhances preexisting precipitating clouds embedded in a frontal system when the system passes over mountains. The dynamical and microphysical mechanisms of the orographic effect vary considerably with the synoptic-scale condition, which has been investigated from various points of view adopting ground-based, airborne, and spaceborne observations; statistical analysis; and numerical models (Overland and Bond 1993; Colle et al. 2006; Olson and Colle 2009; Neiman et al. 2008; Zagrodnik et al. 2018, 2019). This study investigates spatial patterns of precipitation climatology and mechanisms for the south coast of Alaska using two

spaceborne radars, the GPM DPR and CloudSat CPR, to reveal terrain–precipitation interaction at larger spatiotemporal scales.

2. Data and methodology

2.1 Data

The KuPR swath of the normal scan is approximately 245 km wide and comprises 49 beams in the cross-track direction. Each beam has a vertical sampling interval of 125 m and a footprint that is 5 km in diameter. The level-2 version-06A KuPR product (Iguchi et al. 2018) from April 2014 to March 2019 is used in this study. The vertical profile of radar reflectivity and precipitation rate in range bins free from ground clutter and the horizontal dataset of the precipitation flag and rain-type classification products are obtained for analysis. In Section 3, KuPR-detected precipitation events are classified into three types of precipitation, namely, stratiform, convective, and others, using rain-type classification products (Awaka et al. 2016). Although the DPR contains another KaPR having a higher frequency, even in high-sensitivity scanning (HS) of KaPR, the detectability of precipitation is almost comparable with that of KuPR because the non-Rayleigh scattering effect may have partly offset the sensitivity advantage of the KaPR HS over the KuPR (Toyoshima et al. 2015). Therefore, only KuPR products are used in this study.

The CloudSat CPR is a nadir-pointing radar with a vertical resolution of 240 m and footprint dimensions of approximately 1.4 km (cross-track) × 1.8 km (along track). Level-2 CPR products from January 2007 are used in this study, that is, products of the geolocation of footprints, surface bin number, radar reflectivity and CPR cloud mask (2B-GEOPROF; Marchand et al. 2008), precipitation flag and surface type (2C-PRECIP-COLUMN; Haynes et al. 2013), cloud scenario classification (2B-CLDCLASS; Wang and Sassen 2007), and near-surface snowfall rate (2C-SNOW-PROFILE; Wood et al. 2013). Each precipitating event is classified into one of three precipitation phases (i.e., a rain, mixed, or snow phase) at the near-surface bin using the precipitation flag from the 2C-PRECIP-COLUMN product. The precipitation flag in 2C-PRECIP-COLUMN indicates three levels of precipitation probability, namely, "certain", "probable", and "possible", where "certain" is selected in this study. Following Kulie et al. (2016), each cloud-detected event is discriminated into one of three types of cloud scenario using the 2B-CLDCLASS product: nimbostratus, shallow cumuliform (e.g., stratocumulus and cumulus), and other clouds. When using a dataset taken from CPR products, reflectivity data in the four range bins immediately above the surface-containing range bin are excluded to avoid the contamination of surface clutter (Marchand et al. 2008). Furthermore, reflectivity data in range bins with CPR cloud mask values of 20, 30, and 40 are applied, whereas values of 5 at heights lower than 2000 m above the surface are regarded as contaminated by ground clutter and are discarded.

Although the observations of the DPR can cover the target area without gaps owing to scanning in the cross-track direction with a 245-km swath (Fig. 1a), the observation of the CPR is mesh like as shown in Fig. 1b because the CPR observes only at nadir under the geographical constraints of the recurrent orbit of CloudSat. Moreover, the observation time of the CPR is limited by the sun-synchronous orbit of CloudSat passing over a given point on the Earth at the same local times each day, with the equator crossing time of roughly 01:00/13:00 local standard time (LST). Because the local passing time of the satellite with sun-synchronous orbit depends on the latitude of the place, CloudSat overflies the south coast of Alaska around 04:00/14:00 LST. Meanwhile, the non-sun-synchronous orbit of GPM Core allows the DPR to obtain precipitation climatology independent of time. There are further orbital constraints in that after a battery system anomaly in 2011 resulted in some inoperative months, CloudSat entered a sunlight-only operational mode. To avoid the bias of the dataset arising from sampling irregularity in each season and the lack of sampling at night, only the CPR datasets from January 2007 to December 2010 are used in statistical analysis in Section 3.

The synoptic data used in this study to describe the dynamic properties of air flow are from the fifth generation of the European Centre for Medium-range Weather Forecasts Reanalysis (ERA5) products (Hersbach and Dee 2016). The dataset has 0.25° horizontal grid spacing and an hourly temporal resolution. To observe the movement of the upper cloud, the dataset of the cloud-top brightness temperature obtained from the infrared imager ch04 (10.20–11.20 μm) aboard the GOES-15 geostationary satellite is used.

2.2 Distance from the coastline

Datasets from the spaceborne radars and infrared imager in the target region are resampled into 0.1° × 0.1° cells for analysis. For all grid points of both satellite and ERA5 datasets, the distance from the nearest coastline is calculated using the method proposed by Ogino et al. (2016). The dimensions of cells are

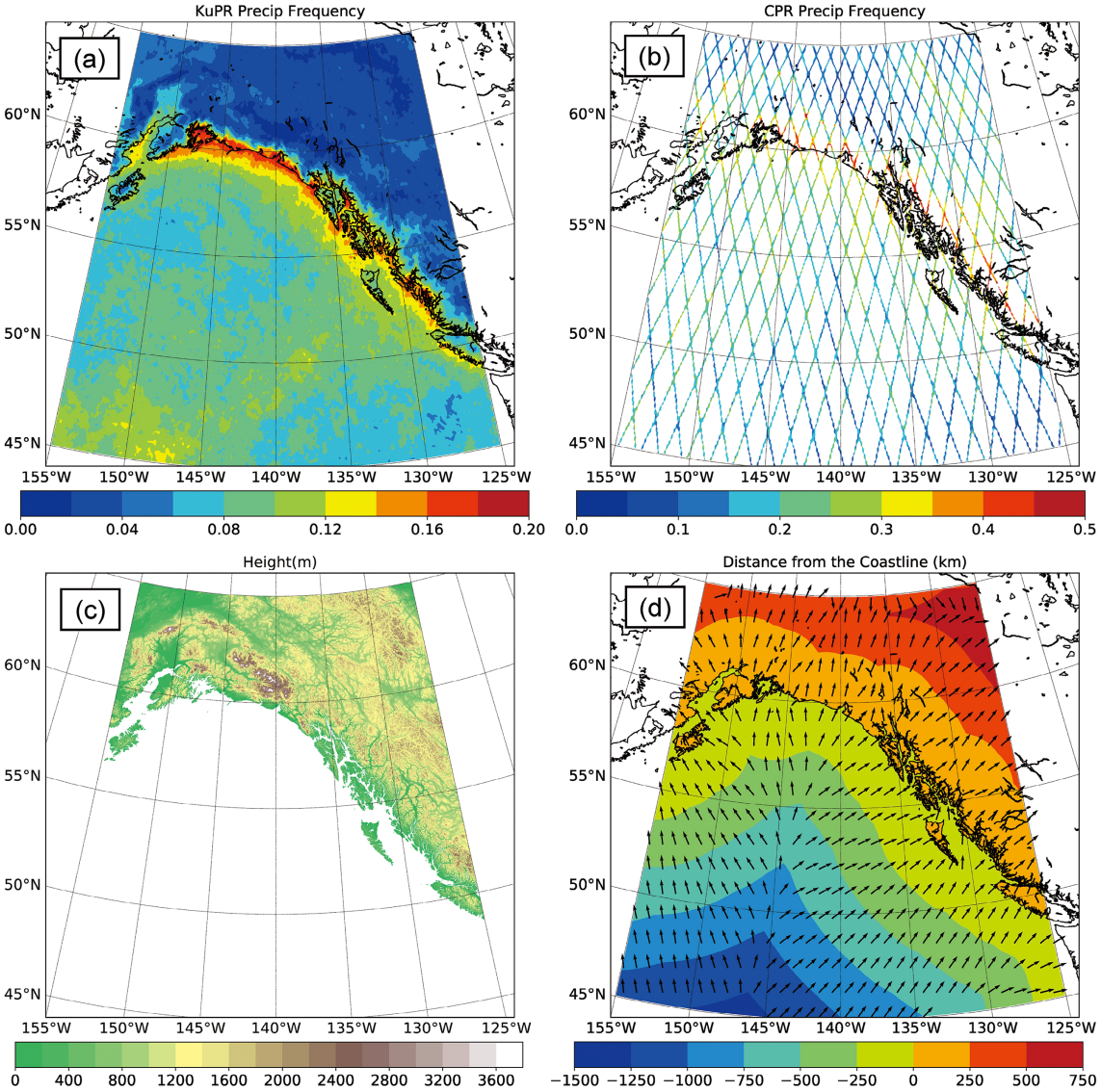

Fig. 1. (a) Five-year-mean KuPR precipitation frequency from April 2014 to March 2019, (b) 4-year-mean CPR precipitation frequency for all types of cloud and all types of precipitation particle phase from January 2007 to December 2010, (c) elevation from SRTM30, (d) (shading) distance from the nearest coastline and (vector) cross-barrier direction around the Gulf of Alaska.

0.1° × 0.1° for spaceborne radar datasets (Figs. 1a, b) and 0.25° × 0.25° for ERA5 datasets. For elevation, Shuttle Radar Topography Mission 30-arc-second data (SRTM30) are used (Fig. 1c). First, if any of the 2 × 2 SRTM30 cells contain both land and ocean cells, the center point of the four cells is specified as a coastline point. Note that lake cells are regarded as land cells. The distance from the nearest coastline point is then calculated for each cell, assuming the Earth to be a sphere with radius of 6,378,140 m (Fig. 1d). Hereafter, all datasets are analyzed by dividing the distance from the coastline by 20 km. In Section 4, the wind in each cell derived from ERA5 is decomposed into cross-barrier and parallel-barrier components. The cross-barrier direction of wind in each cell is obtained adopting the following method. The vector from the center point of the cell to the point of the nearest coastline is first determined and then smoothed with a Gaussian filter

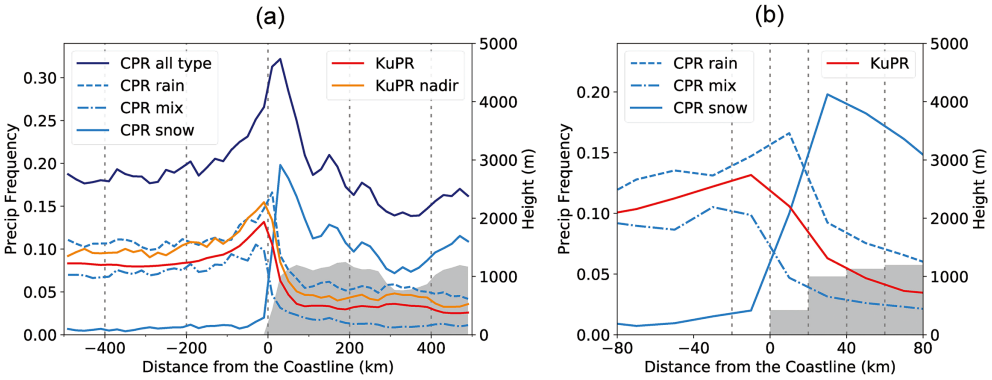

Fig. 2. Relationship between the distance from the coastline and climatological value of precipitation. (a) Four-year-mean CPR precipitation frequency for three types of precipitation particle phase (rain, mixed-phase, and snow) from January 2007 to December 2010 and 5-year-mean KuPR precipitation frequency for all angle and only-nadir observations from April 2014 to March 2019 and (b) an enlarged view of (a). Gray shading represents the average terrain elevation.

having a standard deviation of 2°. Without smoothing, the vector would point toward the protruding shoreline and would not represent the direction to the coastal mountain terrain. The direction of the smoothed vector is referred to as the cross-barrier direction (Fig. 1d). The parallel-barrier direction is obtained by rotating the cross-barrier direction through 90° counterclockwise, and a positive value of the parallel-barrier component thus indicates a wind with a direction such that land is on the right and sea is on the left.

3. Relationship between precipitation and distance from the coastline

3.1 Annual and seasonal precipitation climatology

Figure 2a shows how the frequency of precipitation detected by the two radars changes with distance from the coastline, whereas Fig. 2b shows the enlarged view of coastal areas in Fig. 2a. The term "precipitation frequency" is defined as the ratio of the number of observations for which precipitation was detected to the total number of observations including no-precipitating events. The KuPR-detected precipitation frequency has a peak above coastal water (−20–0 km). The frequency gradually decreases as the distance from the coast on the seaward side increases to 200 km and drops sharply as the distance from the coast on the landward side increases to 100 km (red line in Fig. 2a). As with KuPR, the CPR detects precipitation most frequently near the coastline, and the frequency tends to decrease with distance from the coastline (navy line in Fig. 2a). However, there is a large difference when cases are divided into the three types of precipitation particle phase using 2C-PRECIP-COLUMN. In Fig. 2, the curves of CPR-detected frequencies of rainfall (dashed blue line) and mixed-phase precipitation (dash-dotted blue line) are similar to the curve of the KuPR-detected frequency (red line), in that they are higher over the ocean (from −80 km to 0 km) than over the land (from 0 km to 60 km), and each has a peak near the coastline and a large gradient over the slope of the coastal mountains (from 0 km to 60 km). However, the CPR snowfall frequency (solid blue line) is completely different in that it has a large value landward of the coastline and a peak in the coastal mountain range, whereas the total CPR-detected precipitation frequency (solid navy line) has a peak on the windward side of the coastal mountains (from 20 km to 40 km), more inland from the maximum of the KuPR-detected precipitation frequency.

Spaceborne radars are limited in observing shallow storms and snowfall at low levels owing to ground clutter, which could pose a serious problem for KuPR observation. In the KuPR observation, the bottom levels free from ground clutter largely depend on the incidence angle, being lowest at nadir and highest at the swath's edge (Hirose et al. 2012; Kubota et al. 2016). The mean height of the lowest range bins free from ground clutter for KuPR observations at all incidence angles is approximately 500 m higher than that for KuPR observations at nadir (Fig. 3a). Figure 2a shows that the nadir-only observation (orange line) detects precipitation more often than observations at all other incidence angles (red line), indicating a higher detection of precipitation with a low storm top

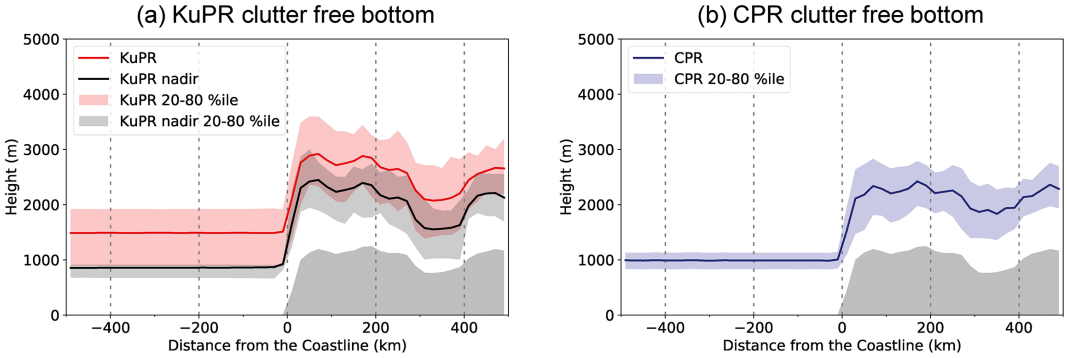

Fig. 3. Relationship between the distance from the coastline and (a) 5-year-mean heights of the lowest range bins free from ground clutter for KuPR observations at all incidence angles and for KuPR nadir-only observations and (b) 4-year-mean heights for CPR observations. Shadings along the solid lines show the range from 20- to 80-percentile values of the heights of the lowest range bins free from ground clutter. The bottom gray shadings represent the average terrain elevation.

height. Even so, the nadir observations have a similar pattern as observations from all other angles, with the maximum value being seaward of the coastline, suggesting that the typical vertical radar profile and the phase of precipitation particles captured by KuPR are independent of the incidence angle of the radar in this region. Thus, KuPR products with all incidence angles are used to ensure a large number of samples when investigating the precipitation climatology in this area. Still in the nadir-only observation, an echo from precipitation particles at heights lower than approximately 1 km from the surface cannot be observed owing to ground clutter obstruction (Fig. 3), which may result in the missing of shallow events especially over mountains with higher levels of clutter-contaminated range bins. This effect may be important at high latitudes because clouds tend to appear at lower heights than they do at low latitudes.

In single-wavelength meteorological radar observations, the properties of precipitation particles are estimated on the basis of radar backscattering from the particles, which is called radar reflectivity. When comparing the detectability of KuPR observation with that of CPR observation, constraints on each dataset should be introduced because the value of KuPR reflectivity cannot be directly interpreted as the value of CPR reflectivity due to differences in the backscattering efficiency of various particle sizes at each radar (Chen et al. 2016; Tang et al. 2017). Figure 3 shows that the mean height of the lowest range bins free from ground clutter is almost the same in both CPR and KuPR observations at nadir, indicating that it is reasonable to compare the precipitation frequency of the KuPR nadir-only observation with that of the CPR observation when identifying precipitation particles in this region. Hereafter, the CPR radar sensitivity is aligned with KuPR at nadir to clarify which type of CPR-detected precipitation can be captured by KuPR. Skofronick-Jackson et al. (2019) compared DPR and CPR snowfall products to clarify disparity in the global average snowfall frequency obtained from the two spaceborne radar datasets. They concluded that the difference can be minimized when CPR observations are artificially truncated below the 8-dBZ near-surface reflectivity threshold. Following Skofronick-Jackson et al. (2019), a CPR precipitation event is excluded if the maximum radar reflectivity in its vertical column does not reach a given threshold. The threshold for maximum radar reflectivity in a vertical column is applied in this study instead of the threshold for near-surface reflectivity used by Skofronick-Jackson et al. (2019); this is because CPR radar reflectivity near the surface is underestimated owing to the attenuation effect of the liquid-phase precipitation particles. The KuPR precipitation frequency at nadir and truncated CPR precipitation frequency are compared while changing the threshold in intervals of 1 dB, and it is found that their disparity over the ocean can be minimized by setting the threshold at 7 dBZ.

The annual and seasonal mean precipitation frequency of KuPR only-nadir observations and 7-dBZ-truncated CPR observations are illustrated in Fig. 4. The KuPR nadir precipitation frequency and CPR liquid precipitation frequency, which is the sum of the CPR rainfall frequency and CPR mixed-phase precipitation frequency, are in good agreement except

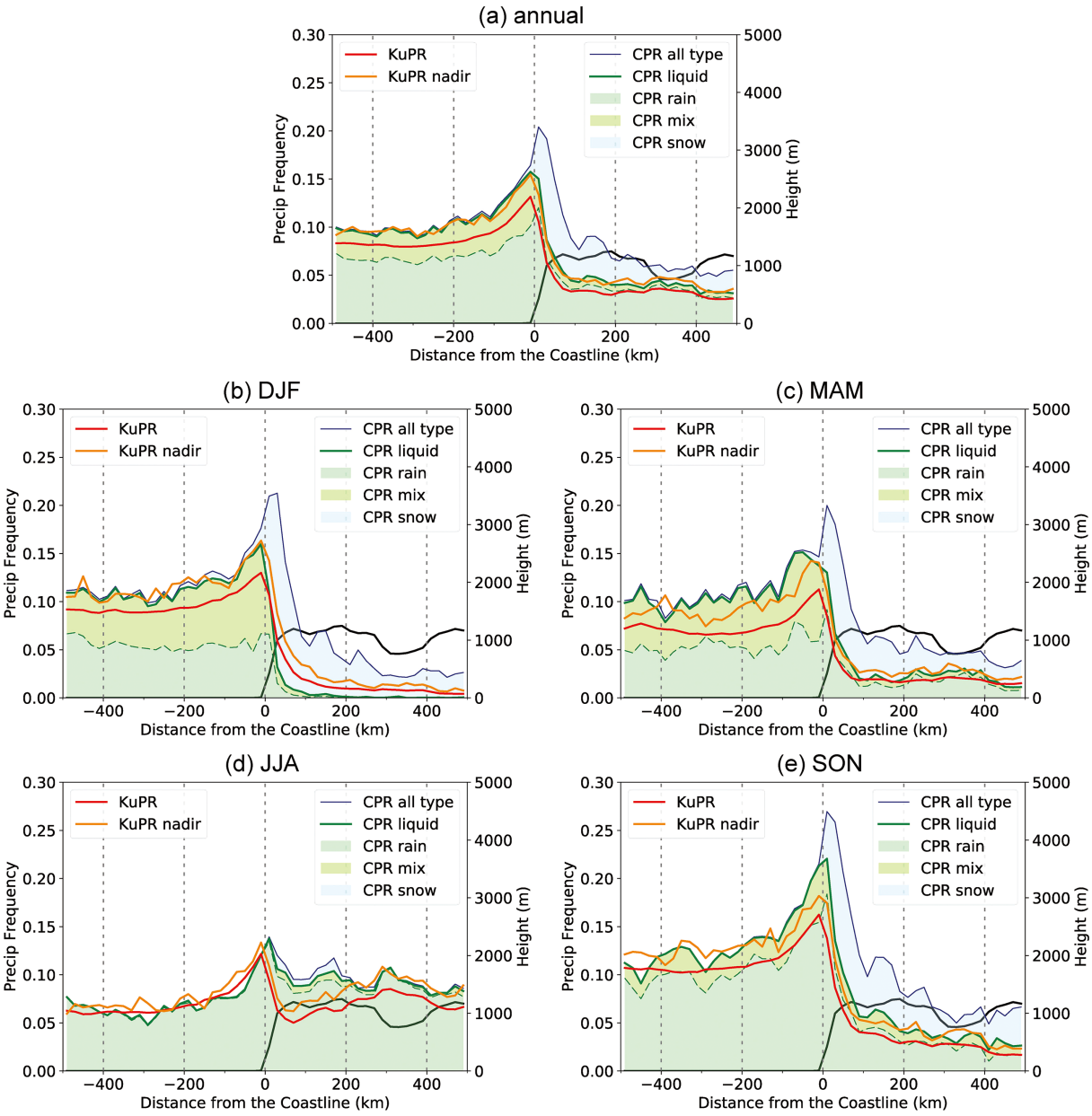

Fig. 4. Same as Fig. 2a but for (a) the annual and seasonal [(b) winter (DJF), (c) spring (MAM), (d) summer (JJA), and (e) autumn (SON)] mean 7-dBZ-truncated CPR precipitation frequency of three types of precipitation particle phase (rain, mixed-phase, and snow) for the period from January 2007 to December 2010. The CPR liquid precipitation is the sum of the CPR rainfall frequency and the CPR mixed-phase precipitation frequency. Black solid lines show the average terrain elevation.

on land in summer (JJA) and winter (DJF) (Fig. 4). Table 1 shows the ratios of the occurrence frequencies of KuPR nadir precipitation and 7-dBZ-truncated CPR precipitation to the frequency of all the precipitation detected by CPR, averaged over the ocean (from −500 km to 0 km) and over the coastal mountains (from 20 km to 280 km; > 1000 m in elevation and not too far from the south coast of Alaska). Table 1 and Fig. 4a reveal that, over the ocean, the frequency of precipitation captured by KuPR nadir observations accounts

Table 1. The ratios of the occurrence frequencies of KuPR nadir precipitation, CPR liquid, CPR snowfall, and 7- and 11-dBZ-truncated CPR precipitation to the CPR total precipitation frequency, averaged over the ocean (from −500 km to 0 km) and over the coastal mountains (from 20 km to 280 km). These thresholds are applied on each types of precipitation detected by CPR. CPR liquid precipitation means the sum of CPR rainfall and CPR mixed-phase precipitation.

	KuPR nadir	CPR		CPR > 7dBZ			CPR > 11dBZ		
		Liquid	Snow	All type	Liquid	Snow	All type	Liquid	Snow
Ocean	55.1 %	95.3 %	4.7 %	56.1 %	54.8 %	1.2 %	30.2 %	29.8 %	0.4 %
Mountain	23.3 %	38.0 %	62.0 %	46.3 %	23.8 %	22.5 %	20.1 %	11.5 %	8.6 %
Mountain (DJF)	14.4 %	5.1 %	94.9 %	36.1 %	3.2 %	32.9 %	14.3 %	1.7 %	12.5 %
Mountain (JJA)	49.1 %	90.4 %	9.6 %	64.0 %	59.5 %	4.5 %	32.5 %	30.4 %	2.1 %

for 55.1 % of that of precipitation captured by CPR, and the percentage is almost the same as the ratio of 7-dBZ-truncated CPR liquid precipitation (54.8 %). Meanwhile, on the coastal mountains, though snowfall events with echoes larger than 7 dBZ (22.5 %) occur as often as liquid precipitation events with echoes larger than 7 dBZ (23.8 %), the ratio of KuPR precipitation on the mountains (23.3 %) is similar as the ratio of 7-dBZ-truncated liquid precipitation (23.8 %). This indicates that KuPR rarely detects snowfall events in coastal mountains.

Over the coastal mountains, the dominant type of precipitation greatly differs depending on the season. Over land in DJF, snowfall accounts for > 90 % of the total precipitation (Table 1). The capture ratio of KuPR is 14.4 % over the coastal mountains in DJF (Table 1), indicating that KuPR cannot detect weak snowfall events and misses approximately 85 % of the total snowfall events captured by CPR due to the weaker backscattering from smaller ice particles. However, Fig. 4b and Table 1 show that the KuPR nadir precipitation frequency (14.4 % in Table 1) is much higher than the 7-dBZ-truncated CPR liquid precipitation frequency (3.2 % in Table 1), suggesting that some heavy snowfall events in DJF can be detected by KuPR. Because 7 dBZ was a threshold concerning seaside liquid precipitation and the minimum detectability of KuPR is expected to differ depending on the type of precipitation particles, another threshold of CPR reflectivity should be introduced concerning snowfall over the coastal mountains. The comparison between KuPR precipitation frequency and truncated CPR precipitation frequency over the coastal mountains in DJF are performed, and it is revealed that the difference between KuPR frequency and truncated CPR precipitation frequency is minimized by setting the threshold at 11 dBZ (14.4 % for KuPR nadir observations and 14.3 % for CPR 11-dBZ-truncated observations in Table 1). Thus, KuPR can detect heavy snowfall events, of which frequency is comparable with that of snowfall events with CPR reflectivity stronger than 11 dBZ. Although the frequency of heavy snowfall events (CPR reflectivity > 11 dBZ) accounts for only 13.2 % (= 12.5/94.9; Table 1) of the total snowfall frequency detected by CPR, the snowfall amount from the heavy snowfall events reaches 47.5 % of the total snowfall amount in DJF when calculated using the near-surface snowfall rate estimated in 2C-SNOW-PROFILE. This indicates that infrequent heavy snowfall events have non-negligible impact on the total snowfall climatology in Alaska, as reported by some precedent studies concerning the global mean snowfall statistics (Casella et al. 2017). This also suggests that KuPR can capture the mass of heavy snowfall events; however, some studies (Casella et al. 2017; Skofronick-Jackson et al. 2019) pointed out that the amount of DPR-detectable heavy snowfall is significantly underestimated in DPR products compared with that in CPR products. Therefore, further research is needed to compare the amount of heavy snowfall estimated by KuPR with the total amount of snowfall estimated by CPR and quantify the contribution of heavy snowfall events.

In contrast to DJF, liquid precipitation accounts for > 90 % in JJA. The KuPR precipitation frequency over the coastal mountain in JJA is about a half of the CPR precipitation, indicating that KuPR can capture much more liquid precipitation than snowfall. However, Table 1 and Fig. 4d show that the percentage of KuPR nadir precipitation frequency (49.1 %) does not reach the percentage of 7-dBZ-truncated CPR liquid precipitation frequency (59.5 %), which may be due to an abundance of smaller rainfall particles and KuPR missing some isolated shallow rainfall events in the mountains, owing to KuPR (5 km) having a larger footprint than the CPR (1 km). Besides, the disparity may arise because CPR observation only at 04:00 and 14:00 LST cannot accurately represent the diurnal variability during JJA.

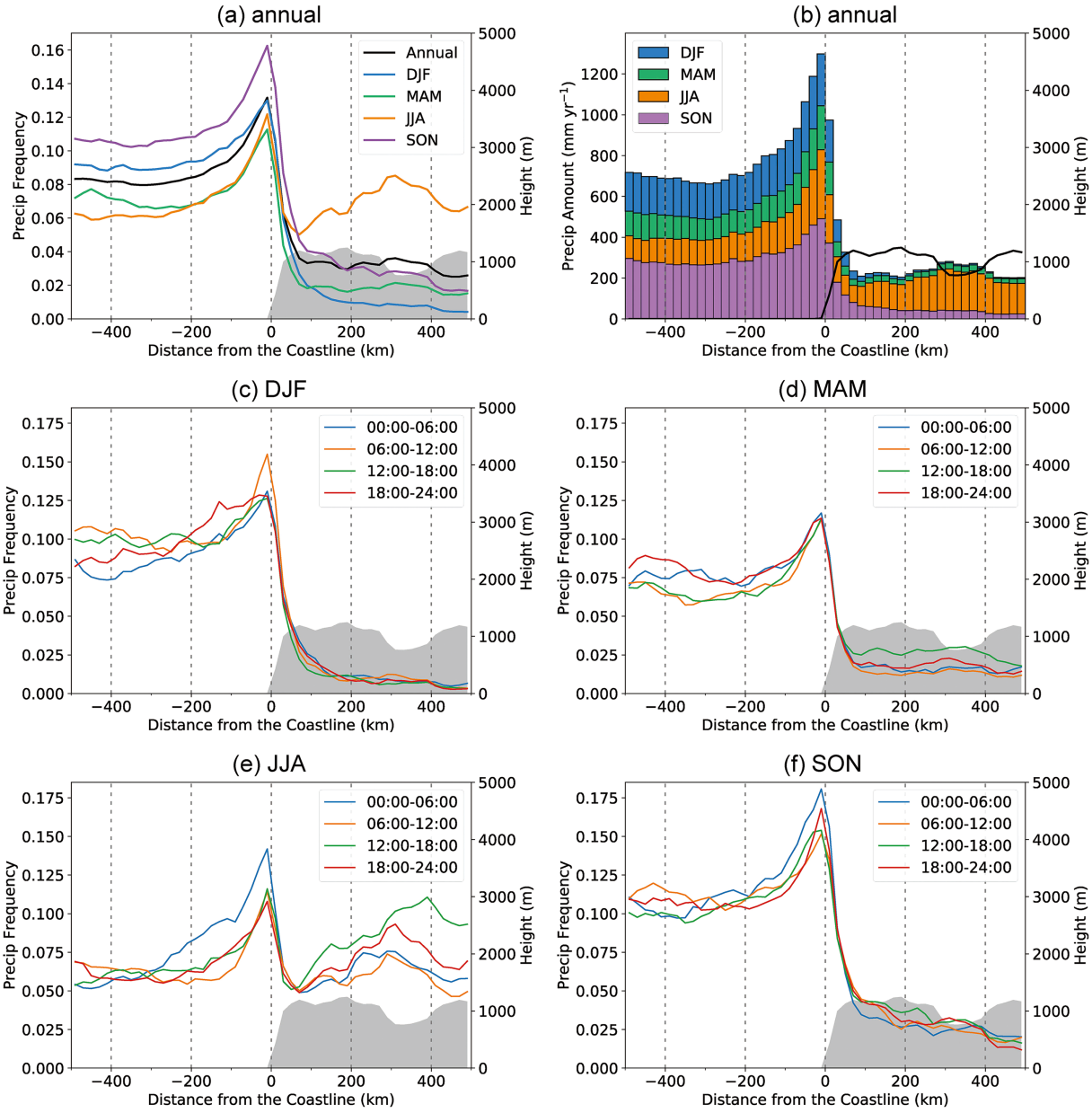

Fig. 5. Same as Fig. 2a but for the 5-year seasonal mean of the (a) KuPR precipitation frequency and (b) KuPR precipitation rate and the 6-hourly diurnal variation of the precipitation frequency in (c) winter (DJF), (d) spring (MAM), (e) summer (JJA), and (f) autumn (SON) shown with local standard time (LST). A black solid line in (b) shows the average terrain elevation.

Figures 5a and 5b shows that both the KuPR-detected precipitation frequency and amount are highest in autumn (SON). The Gulf of Alaska, which is the so-called graveyard of Pacific storms, has a high storm track density, and extratropical cyclones more frequently exist in the Gulf of Alaska, especially in autumn (Mesquita et al. 2010). These results indicate that the coastal mountains delay fronts approaching the coastline and dam southwesterly moist air flows associated with extratropical cyclones in the Gulf of Alaska, and most of the moisture condenses over the sea and lowlands near the coast to produce precipi-

tation. Figures 5c–f shows the diurnal variability of the precipitation frequency in each season. There is only small diurnal variability during the SON, DJF, and spring (MAM) periods, and this is consistent with the fact that precipitation from synoptic-scale cyclonic activity, which has time scales longer than a day, is dominant in these seasons (Figs. 5c, d, f). In JJA, there is not only a coastal maximum but also a secondary maximum over land approximately 300 km from the coastline (Figs. 5a, b), and these peaks have diurnal variations (Fig. 5e). Figure 5e shows that the interior peak of precipitation in JJA is most frequent in the afternoon (12:00–18:00 LST), indicating that the daytime heating of land by solar radiation may contribute to the inland precipitation during summer. Over the ocean, the KuPR precipitation frequency is a maximum in the early morning (00:00–06:00 LST). In tropics, the continental rainfall maximum in the afternoon and oceanic rainfall maximum in the early morning are prevailing diurnal features of precipitation; this has been well studied using TRMM PR data (Kikuchi and Wang 2008). The diurnal variation of rainfall around the south coast of Alaska may have a cause similar to that in the tropics (e.g., the effect of the thermal land–sea breeze and mountain–valley breeze), though further analysis must accurately identify the cause because the underlying forcing mechanisms of the diurnal variation of rainfall differ from place to place (Yang and Smith 2006). Still in JJA, the maximum precipitation peak appears on coastal water at any time, and the diurnal variation over the ocean is relatively small compared with the total precipitation (Fig. 5e). This climatological distribution differs from the tropical climatology strongly dominated by diurnal rainfall regimes, as suggested by previous studies for the Indonesian Maritime Continent (Mori et al. 2004; Yamanaka 2016) and northwestern South America (Mapes et al. 2003a, b). In some areas of the tropics such as Western Ghats in India and Arakan Yoma in Myanmar where the summer-time low-level monsoon flow is strong, diurnal variations in precipitation are weak despite the large rainfall amount due to continuous environmental flow perpendicular to coastal mountains (Shige et al. 2017). As in these areas, the small diurnal amplitude of precipitation over the coastal waters of Alaska (Fig. 5e) suggests that the summer-time precipitation climatology is strongly affected by synoptic water vapor transported from the ocean, though the transport is associated not with monsoon flow but with moisture intrusion around extratropical cyclones.

To determine which types of cloud play an important role in coastal precipitation, each precipitating event detected by the CPR is classified into one of three types of cloud scenario, namely, nimbostratus, shallow cumuliform, and other clouds, following Kulie et al. (2016). Figures 6a and 6b indicates that, among the clouds captured by the CPR, nimbostratus clouds most frequently bring precipitation to each targeted region and they are the main source of snowfall in the mountains. The snowfall rate shown in Fig. 6b is low over the ocean because precipitation particles mainly fall as rain or mixed-phase precipitation rather than as snow (Fig. 2a). The amounts of CPR rainfall and mixed-phase precipitation are not shown in Fig. 6b because they are difficult to estimate only from CPR reflectivity, owing to liquid particles strongly scattering the beam and causing saturation of the attenuation signal. To reveal which type of cloud brings such a large amount of rainfall over the ocean, KuPR-detected precipitation events are classified into three types of precipitation, namely, stratiform, convective, and other, using the KuPR rain-type classification (Figs. 6c, d). Although the nimbostratus clouds observed by the CPR may not perfectly match the stratiform rainfall observed by KuPR in some cases because the classification methods differ, these clouds are precipitating clouds with the same properties because they are characterized by both weak intensity and a wide extension in areas compared with convective precipitation in each product. According to Figs. 6c and 6d, stratiform precipitation accounts for > 80 % of the total precipitation in terms of both frequency and amount, suggesting rainfall and mixed-phase precipitation are mainly brought by the stratiform cloud system. Therefore, precipitation in this region is mostly brought as stratiform precipitation, which may fall from nimbostratus clouds, and is related to frontal cloud systems associated with extratropical cyclones.

3.2 CFAD analysis

To show how precipitation characteristics differ according to the distance from the coastline, reflectivity data obtained from KuPR and the CPR when precipitation is detected by each radar are aggregated into contoured frequency and altitude diagrams (CFADs; Yuter and Houze 1995) for five geographic regions according to the distance from the coastline: from −80 km to −20 km and every 20 km from −20 km to 60 km. In these regions, there are large gradients of precipitation frequency detected by spaceborne radar (Fig. 2b). The CFADs are two-dimensional histograms of KuPR (CPR) reflectivity profiles with the horizontal axis representing reflectivity from 0 to 50 dBZ

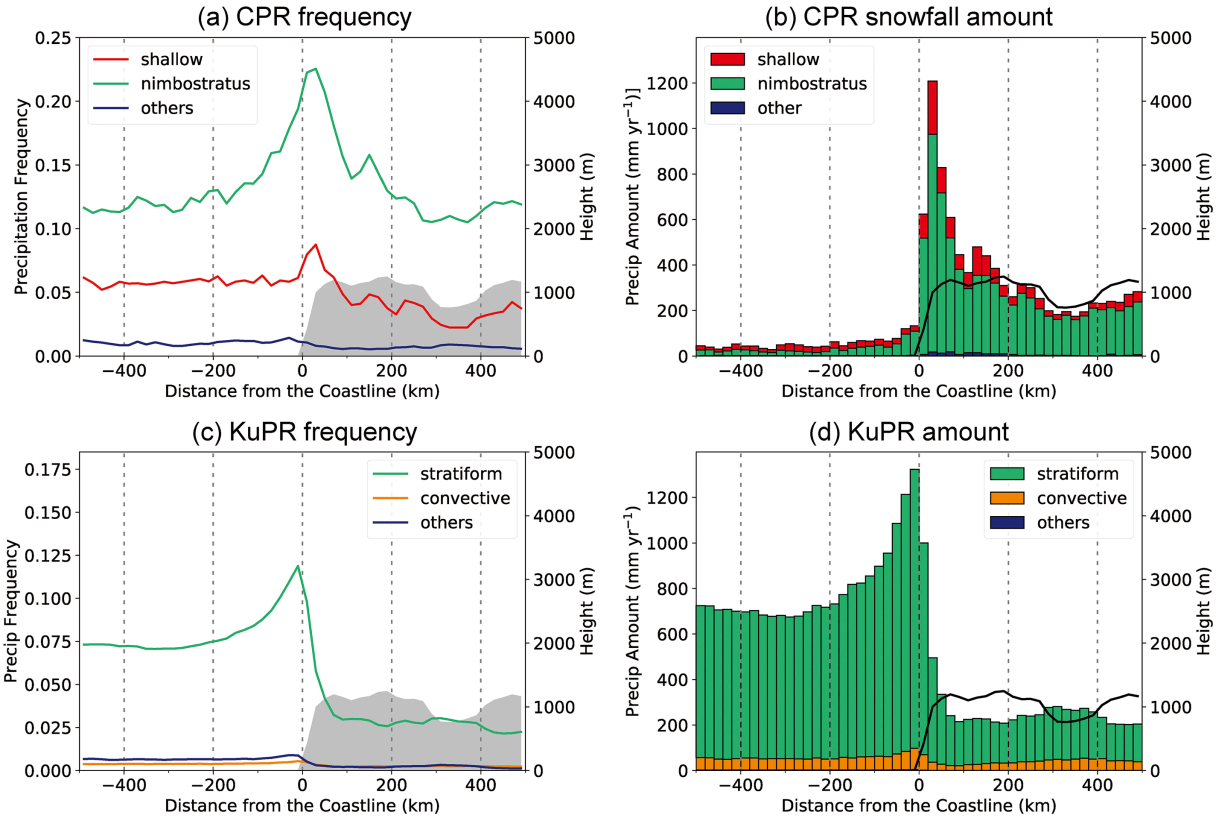

Fig. 6. Same as Fig. 2a but for (a) the 4-year-mean CPR precipitation frequency for three types of precipitating cloud (shallow cumuliform, nimbostratus, and others), (b) CPR snowfall rate for the three types of cloud, (c) 5-year-mean KuPR precipitation frequency, and (d) amount for three types of precipitation (stratiform, convective, and others). Gray shadings in (a, c) and black solid lines in (b, d) show the average terrain elevation.

(from −30 dBZ to 25 dBZ) in intervals of 1 dBZ and the vertical axis representing altitude from 0 km to 10 km in intervals of 125 m (240 m). Each CFAD is normalized by the number of observations at each height including non-precipitating events. Because bins near the surface have a lower sampling number than upper bins owing to ground clutter obstruction, bins at the lower level having a sampling number < 20 % of that of the upper level are discarded.

A large fraction of precipitation echoes are observed above coastal water (from −20 km to 0 km in Fig. 7a) corresponding to the location where the KuPR-detected precipitation frequency has its maximum in Fig. 2b. In landside regions (from 0 km to 60 km in Fig. 7a), the KuPR reflectivity weakens, and the echo top height falls, going inland. Although shallow events may be underestimated because the lowest range bin free from surface clutter is higher over land, the weakening of the echoes is also clear at a height of ≥ 3 km (from 0 km to 60 km in Fig. 7a), where the effect of ground clutter is weak (Fig. 3a), showing that inland precipitation weakens with increasing distance from the coastline.

Although KuPR suffers from the underestimation of light precipitation, KuPR has advantages over the CPR in observing heavier precipitation. The vertical profiles of KuPR reflectivity in Fig. 7a show that the intensity of reflectivity generally increases downward, and this feature is especially clear over the coastal ocean and lowlands (from −80 km to 20 km). Meanwhile, the reflectivity of CPR-detected echoes in the area corresponding to the echo observed by KuPR (CPR-detected reflectivity exceeding 7 dBZ and height < 3 km in Fig. 7b) no longer increases downward; this is because the strong backscattering from liquid particles causes the saturation of attenuation signals in CPR observation (Berg et al. 2010; Chen et al. 2016). Thus, it is difficult for the CPR to distinguish atten-

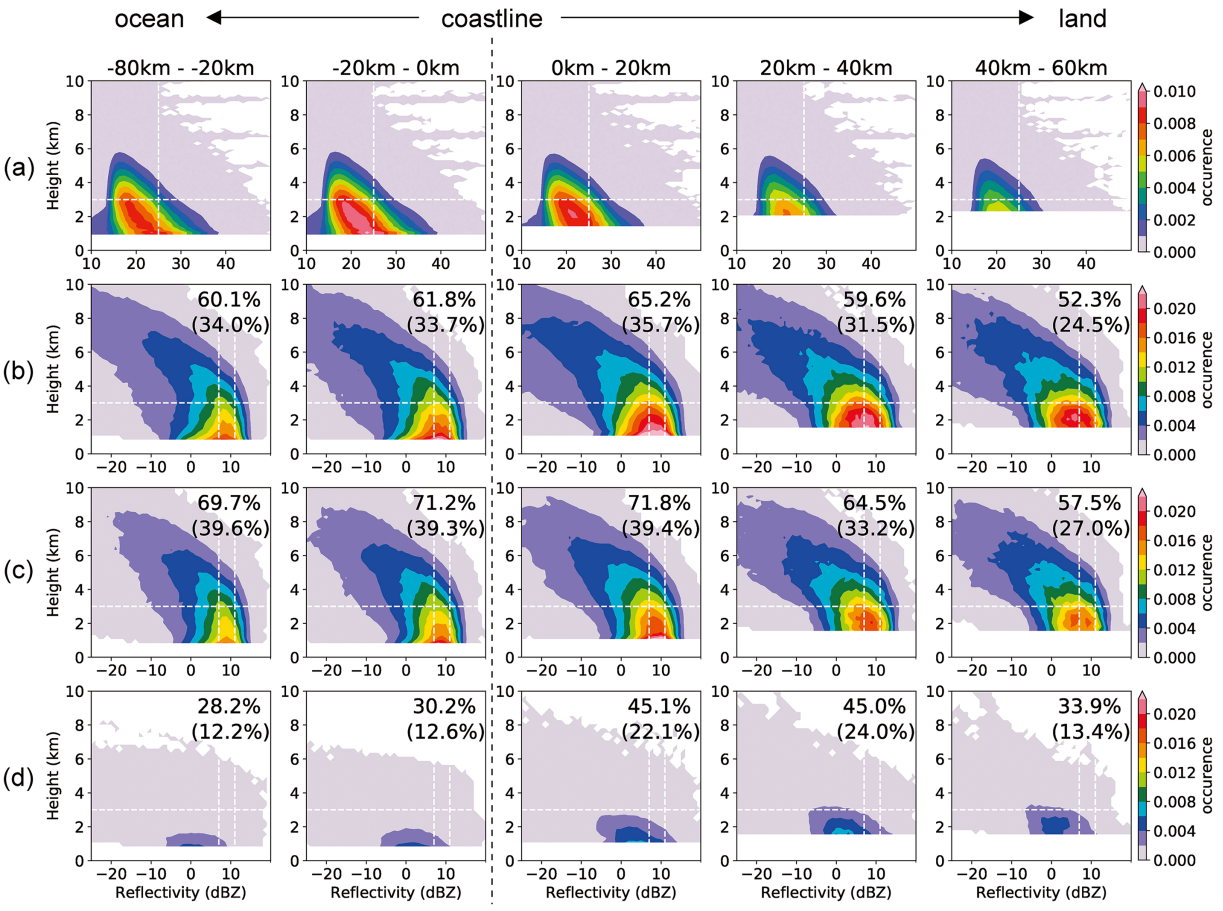

Fig. 7. CFADs of (a) the 5-year-mean KuPR reflectivity and the 4-year-mean CPR reflectivity of (b) all, (c) nimbostratus, and (d) shallow cumuliform cloud types when precipitation is detected for different distances from the coastline. Two-dimensional histograms of the reflectivity profile with intervals of 1 dB and a vertical resolution of (a) 125 m and (b–d) 240 m. Each CFAD is normalized by the number of observations in the respective area. White dashed vertical lines at reflectivity of 7 dBZ (11 dBZ) in (b–d) indicate the threshold at which KuPR detects the echo over the ocean (over the coastal mountains). For all CFADs of the CPR, the ratio of the number of profiles with echoes stronger than the 7-dBZ and 11-dBZ thresholds to the total number of observed profiles is calculated and shown in the upper right of each CFAD. (The ratio when the 11-dBZ threshold is applied is shown in parentheses.) White dashed horizontal lines at a height of 3 km and vertical lines at 25 dBZ in (a) are drawn for reference.

uated echoes of moderate–heavy precipitation from echoes of light precipitation. These results illustrate that the use of Ku-band radar is important in estimating the precipitation amount in relatively heavy events that frequently occur near the coast.

A comparison of CFADs of the CPR in Fig. 7b with those of KuPR in Fig. 7a shows that the CPR detects cloud and precipitation particles to a higher altitude and more frequently than KuPR. In Section 3.1, it was shown that the difference in precipitation frequency detected by the two radars over the ocean (over the coastal mountains) can be minimized when CPR observations are artificially truncated below a reflectivity threshold of 7 dBZ (11 dBZ). To quantify the proportion of profiles with strong echoes, the ratio of the number of profiles with echoes stronger than 7 dBZ (11 dBZ) to the total number of observed profiles is shown for each CFAD of the CPR in Fig. 7. CFADs of the CPR for all cloud types (Fig. 7b) show that, on the sea side of the coastline, the ratio of profiles with reflectivity stronger than the 7-dBZ threshold gets higher as the distance from the coastline decreases (from −80 km to 0 km; 60.1–61.8 %) and has its maximum at coastal lowlands (from 0 km to 20 km;

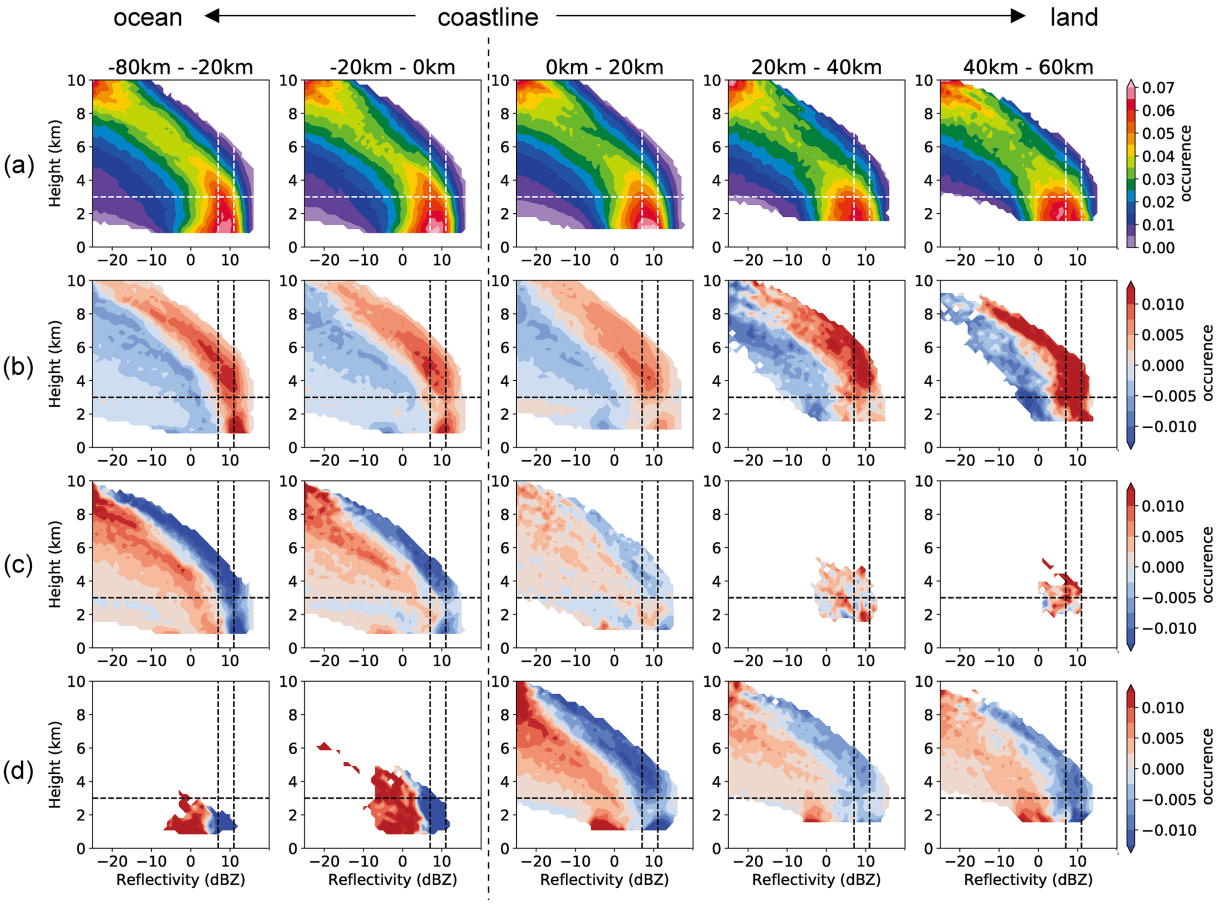

Fig. 8. CFADs of the 4-year-mean CPR reflectivity of (a) all precipitation, (b) rainfall, (c) mixed-phase precipitation, and (d) snowfall from nimbostratus clouds, normalized by the number of observations at each height for the respective area. The frequencies of occurrence shown in (b–d) are expressed as the deviation from (a). The horizontal and vertical intervals are the same as those in Fig. 7. Data in a cell of a CFAD with fewer than 100 observations are discarded.

65.2 %). In contrast, over the coastal mountains (from 20 km to 60 km), the ratio gets lower as the distance from the coastline increases, such as 59.6 % from 20 km to 40 km and 52.3 % from 40 km to 60 km, indicating increase in the number of echoes with weak reflectivity.

Precipitating events captured by the CPR are classified by CPR cloud scenario classification to present the CFADs of nimbostratus clouds in Fig. 7c and those of shallow cumuliform clouds in Fig. 7d. Nimbostratus clouds are relatively thick (≥ 4 km in mean thickness) precipitating clouds with a broad horizontal extent according to 2B-CLDCLASS classification (Wang and Sassen 2007), and they tend to have larger values of CPR reflectivity throughout the area (57.5–71.8 % profiles with echoes larger than 7 dBZ; Fig. 7c). The CFADs of nimbostratus clouds in Fig. 7c have similar patterns as those of all clouds in Fig. 7b especially in an area with stronger reflectivity, suggesting that nimbostratus clouds bring most of the precipitation in this region including over the ocean. To make clear the differences in vertical structure of clouds among different distances from the coastline, CFADs of nimbostratus clouds are normalized by the number of observations when precipitation echoes are detected at each height (Fig. 8a). Figure 8a shows that inland echoes with reflectivity weaker than 7 dBZ more often appear in layers of the lowest 3 km with increasing distance from the coastline (from 0 km to 60 km in Fig. 8a). This suggests that nimbostratus clouds tend to get weaker as these clouds enter the coastal mountains. Meanwhile, echoes from shallow cumuliform

clouds are infrequent and weak (28.2–45.1 % profiles with echoes larger than 7 dBZ; Fig. 7d) compared with those from nimbostratus clouds, showing that few of the shallow cumuliform clouds are associated with precipitation owing to the weak reflectivity, though they are slightly enhanced above the coastal mountains. In Fig. 7d, some clouds are classified as shallow cumuliform clouds, namely, cumulus and stratocumulus clouds (Section 2), with a top height of 10 km over land. This is because the maximum height of cumulus clouds reaches approximately 7 km from the ground surface in some cases according to the classification scheme in 2B-CLDCLASS (Wang and Sassen 2007), and there are locations in the coastal mountainous area having an elevation of $\geq$ 3000 m. These cases are so rare that we consider the effect on the overall statistics to be negligible and we sum the data without removing these cases.

Though Fig. 7c shows that the increasing echoes with weak reflectivity contributes to the concentration of precipitation on coastal mountains, it also illustrates that CPR more frequently detects stronger echoes of > 7 dBZ over the mountains (from 20 km to 60 km) than those over the ocean (from −80 km to 0 km). However, KuPR-detected echo intensity and frequency are remarkably reduced on the coastal mountains. To reveal the cause of the considerable difference in the liquid/solid precipitation frequency and disparity in precipitation products from KuPR and the CPR, CFADs of nimbostratus clouds for each phase-type of precipitation are presented in Figs. 8b–d. In these figures, occurrence frequencies are expressed as the deviation from the CFADs of all types of precipitation phases in Fig. 8a. In each region, rainfall tends to have greater reflectivity than mixed-phase precipitation and snowfall throughout the vertical profile, and more echoes from rainfall particles above a height of 3 km exceed the 7-dBZ threshold, indicating rainfall is more likely to be detected by KuPR than other phases of precipitation (Fig. 8b). Over the coastal mountains, the number of rainfall events is about half that of snowfall as shown in Fig. 2b, and thus, the concentration of precipitation mainly results from snowfall. Meanwhile, the snowfall profiles show echoes more often in the area with reflectivity lower than 7 dBZ (Fig. 8d) compared with rainfall and mixed-phase precipitation (Figs. 8b, c). Though there are some snowfall events exceeding 7 dBZ, which correspond to the increasing stronger echoes (> 7 dBZ) on the coastal mountains in Fig. 7c, most of the snowfall echoes do not reach 11 dBZ in reflectivity, which is KuPR's threshold in detecting snowfall (Section 3.1). Reflecting this fact, the ratio of profiles with echoes weaker than 11 dBZ on the mountains comprise approximately 70 % of the nimbostratus clouds detected by CPR (from 20 km to 60 km in Fig. 7c), indicating the dominance of light-to-moderate snowfall. Because light-to-moderate snowfall (with reflectivity lower than 11 dBZ) is well detected by CPR but rarely detected by KuPR, there exists a large difference in detectability between KuPR and CPR over the coastal mountains.

4. Discussion

Section 3 showed that the south coast of Alaska receives relatively heavy and consistent precipitation and has a large gradient of precipitation. This section discusses how these tendencies appear. Previous studies (Neiman et al. 2008; Zagrodnik et al. 2018) showed that precipitation along the mid-latitudinal western coasts of continents is brought by frontal systems and moisture inflow associated with synoptic-scale eddies, which are Aleutian lows in the case of Alaska, and these preexisting systems may be affected by underlying coastal mountains, causing such large gradients of precipitation properties detected by the KuPR and the CPR (Fig. 2).

Shading in Fig. 9a shows the vertical profile of the 5-year-mean unconditional precipitation rate (i.e., the mean of all precipitation rates including the zero rate) from the level-2 KuPR product as a function of the distance from the coastline. In Fig. 9, bins at the lower level having a sampling number of KuPR (CPR) < 10 % (20 %) that of the upper level are discarded. From ERA5, mean cross-barrier and parallel-barrier components of wind when precipitation events are observed at the location at which the KuPR precipitation frequency is a maximum (−20–0 km) are also drawn. Above the ocean, the cross-barrier component of the low-level wind (lower than approximately 2 km) weakens as it approaches the coastline, indicating convergence due to the orographic blocking of air flow. As a result of the convergence of moist air flow, the mean precipitation rate increases and the precipitation top height rises while approaching the coastline over the ocean (Fig. 9a). Over the coastal mountains (20–80 km), the precipitation rate measured by the KuPR decreases drastically because KuPR cannot observe snowfall or weak shallow rainfall over the coastal mountains (Section 3). Precipitation detected by the KuPR largely occurs at a level lower than the mean height of a temperature of 0°C (thick black line in Fig. 9a), implying precipitation particles mainly fall as rainfall on coastal ocean and lowlands.

Figures 9b–d shows 4-year-mean vertical profiles

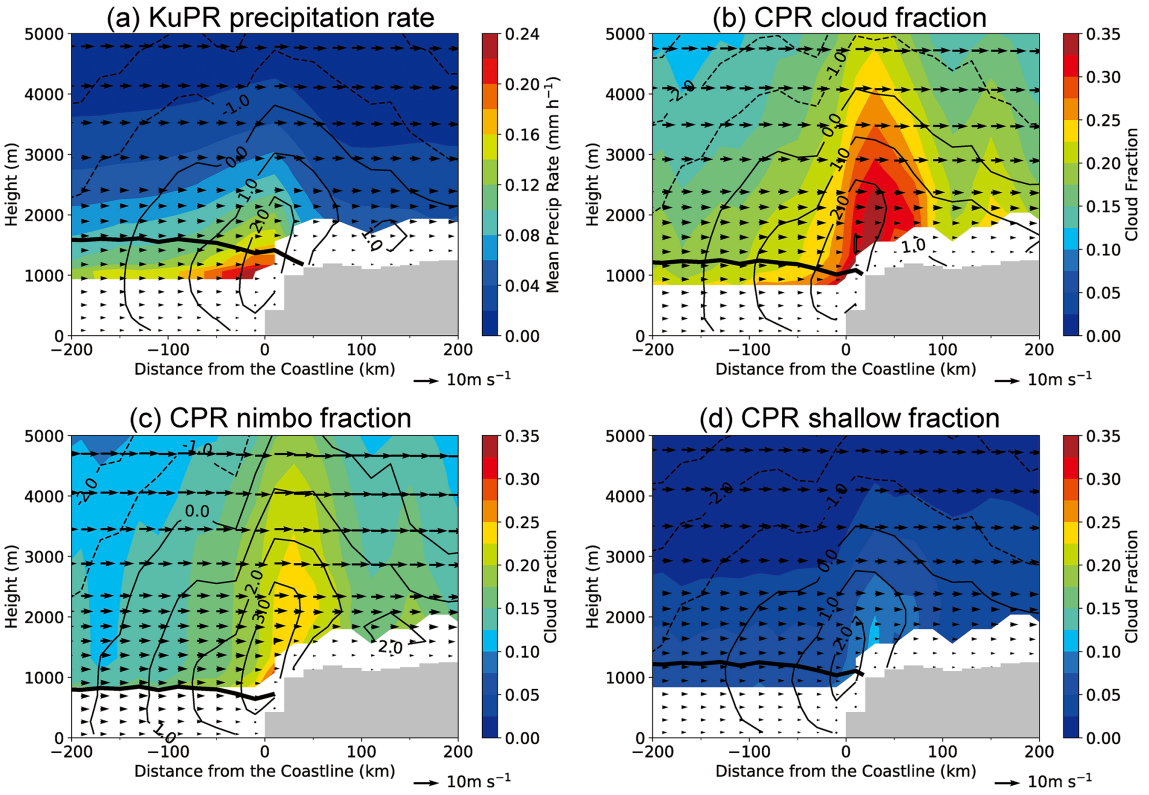

Fig. 9. Relationship between the distance from the coastline and vertical profiles of precipitation, cloud from spaceborne radars, and wind from ERA5. Shading shows (a) the mean precipitation rate from the 5-year observation of the KuPR and (b) total, (c) nimbostratus, and (d) shallow cumuliform cloud fractions when precipitation is detected in near-surface bins from the 4-year observation of the CPR. Vectors show the mean cross-barrier component of wind, and contours show the mean parallel-barrier component of wind with an interval of 1 m s^{-1} when precipitation events are observed in the areas (a) from −20 km to 0 km [(b–d) from 20 km to 40 km] where the KuPR (CPR) precipitation frequency is a maximum. A positive value of the cross-barrier component indicates a wind direction from sea to land, whereas a positive value of the parallel-barrier component indicates a wind direction with land on the right and sea on the left. Thick black lines show the mean height of a temperature of 0°C obtained from ERA5. Height ranges at the lower level having fewer than 10 % (20 %) of KuPR (CPR) observations at the upper level are discarded.

of the precipitating cloud fraction (i.e., the ratio of the number of cloud appearance when precipitation is detected at the near-surface to the number of observations including no-cloud events) from the CPR observation. The panels also illustrate the mean cross-barrier (vector) and parallel-barrier (contour) component winds from ERA5 when precipitation is detected at the location where the CPR precipitation frequency is a maximum (20–40 km). Nimbostratus clouds, which are the dominant producer of snowfall in the region (Section 3), most frequently appear along the coastal mountains (20–80 km in Figs. 9b, c), where the KuPR captures less precipitation (Fig. 9a). In contrast to winds at a lower level, the cross-barrier components of upper winds are no longer weakened by the underlying terrain (vectors in Fig. 9). It is inferred that the clouds primarily forming along the coastline with abundant water vapor yield a large amount of precipitation before reaching the mountains, and the remnants are swept by the upper wind and drift over the coastal mountain range. Around the windward side of the coastal mountains, the parallel-barrier component of the wind strengthens as the cross-barrier component of low-level wind weakens. This enhancement of parallel-barrier wind not only ensures clouds around the coast to stay longer but also provides additional moisture from lower latitudes, yielding the long-lasting precipitation in this region. Shallow cumu-

liform clouds appear when cross-barrier winds and moisture convergence are relatively weak (Fig. 9d). Figure 7d shows that reflectivity from this type of cloud is typically low, and the contribution of this cloud to the amount of snowfall in the mountains is not large (Fig. 9d), though it accounts for a large part of the distribution of the cloud fraction detected by the CPR. The mean heights of the coastal mountains are close to the freezing level (thick black lines in Figs. 9b–d), and the precipitation particles thus fall as rainfall and mixed-phase precipitation on the ocean but as snowfall in the coastal mountains (Fig. 2b).

The precipitation mechanism deduced from the climatological picture in Fig. 9 is recognized in a case study presented in Fig. 10. Figure 10 shows the time series of a case lasting from 00:00 UTC on 13 December to 23:30 UTC on 17 December 2014, when an occluded front and moist air flow accompanied by low pressure approached the south coast of Alaska from the ocean. Datasets shown in Fig. 10 are derived from ERA5, except for infrared imagery taken from GOES-15 in Fig. 10d and spaceborne radar data in Figs. 10e and 10f. Although spaceborne radars capture the vertical structure of clouds and precipitation with more detailed horizontal and vertical resolution than ERA5, they can only observe a limited area of the entire target region at certain time intervals determined by the orbital property of the satellites. Because ERA5 covers the entire target region every hour, it can continuously track the temporal development of a synoptic-scale phenomenon. ERA5 is thus used to clarify how the precipitation events caught by spaceborne radars were generated on a synoptic-scale. In the Supplement, the vertical profile of each radar is presented with the coincident ERA5 reanalysis profile for a case on 14 December 2014, showing that precipitation captured by KuPR and clouds captured by the CPR are largely reproduced in the reanalysis products, though ERA5 has difficulty reproducing fine structures along the terrain and shallow clouds over the sea.

The convergence zone of wind at a lower level (hatches in Fig. 10a) corresponding to an occluded front proceeded from the ocean and reached the coast on the morning of December 15. Near the coastline, there was another weak convergence zone due to the orographic effect before the front arrived, and it strengthened when the convergence zone from the ocean reached the coastline (hatches in Fig. 10a). The air with a large amount of total-column water moved toward the coastline slightly ahead of the low-level convergence zone (shading in Fig. 10a). This moist area corresponded to moisture flow in a warm sector of an extratropical cyclone (Fig. 8 of Houze et al. 2017). Low-level winds formed in the parallel-barrier direction rather than in the cross-barrier direction, resulting in a continuous inflow of moisture from upwind of the parallel-barrier flow or lower latitude (vectors in Fig. 10b). Shading in Fig. 10b shows that the vertically integrated divergence of moisture flux, which is the superposition of the two values in Fig. 10a, continued to converge from the late night of 13 December to the morning of 17 December. This means that most of the moisture that was advected from the ocean was blocked by coastal mountains and consumed to produce terrain-enhanced long-lasting precipitation along the coastline (Fig. 10c). Figures 10e and 10f presents the precipitation rate from KuPR and type of precipitating clouds from the CPR. Corresponding to the precipitation rate from ERA5 (Fig. 10c), KuPR observed the approaching precipitation associated with an occluded front and the orographic enhancement around the coastline (Fig. 10e), and the CPR-detected the coastal precipitation as nimbostratus clouds (Fig. 10f). In the cold-air inflow area behind the front (from −1000 km to −500 km at 00:00 UTC on 15 December and from −1000 km to −250 km at 00:00 UTC on 16 December), many shallow cumuliform clouds are observed by the CPR, and there is not much precipitation for either KuPR or ERA5. The observed brightness temperature of the upper cloud from GOES-15 penetrated inland without being blocked by the terrain (Fig. 10d). This indicates that the upper part of the precipitation cloud that strengthened above the coastline was swept away by the upper wind and advected to the coastal mountainous area in contrast with the situation for the lower layer. Precipitation generated by this series of clouds may result in snowfall in the coastal mountains and correspond to the series of nimbostratus clouds observed by the CPR as shown in Fig. 9c.

5. Summary

The precipitation climatology and mechanism along the south coast of Alaska were investigated, focusing on large spatial gradients of precipitation around the western coast of the continent at mid–high latitude. At higher latitudes, discriminating the phase of precipitation particles falling on the ground is also important in grasping the hydrological cycle in a region, whereas only the amount of precipitation is important in tropical areas. Using complimentary datasets from the GPM DPR and CloudSat CPR, we studied how the horizontal and vertical distributions of precipitation

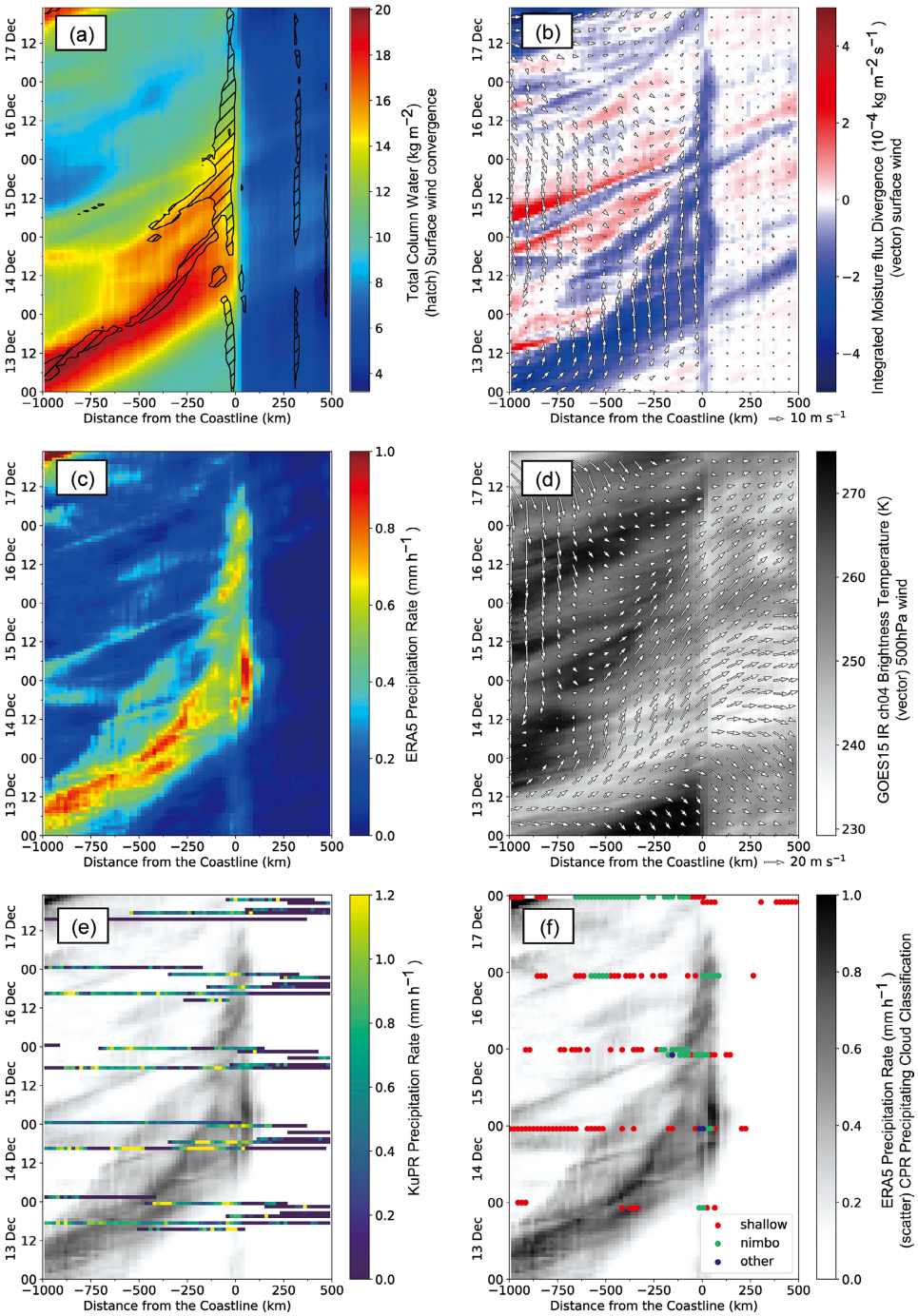

Fig. 10. Time–distance diagrams of an approaching front and moist air flow for a case from 0:00 UTC 13 December to 23:30 UTC 17 December 2014. (a) (Shading) Total-column water and (hatch) the area divergence of surface wind $< -2.0 \times 10^{-5}$ m^{-2} s^{-1}, (b) (shading) divergence of vertically integrated moisture flux and (vector) surface wind vector, (c) precipitation rate from ERA5, (d) (shading) GOES-15 infrared ch04 brightness temperature and (vector) 500-hPa wind vector, (e) KuPR precipitation rate, and (f) CPR precipitating cloud type. Gray shading in (e) and (f) shows the precipitation rate from ERA5. The horizontal component of vectors represents the cross-barrier component of the wind velocity, whereas the vertical component of vectors represents the parallel-barrier component of the wind velocity.

and clouds change with distance from the nearest coastline and made the following conclusions:

(1) KuPR and the CPR have different scattering properties and can thus be used to detect different precipitation particles. This study found that KuPR captures CPR-detected rainfall and mixed-phase precipitation with higher reflectivity (specifically, $\geq$ 7 dBZ CPR reflectivity), and the capture ratio of KuPR corresponds to approximately 50 % of the total liquid precipitation detection by CPR. However, KuPR hardly captures CPR-detected snowfall (approximately 15 % of the CPR snowfall events) and misses large parts of light-to-moderate snowfall prevailing on the coastal mountains of Alaska, though KuPR captures snowfall events as often as CPR-detected heavy snowfall events with reflectivity stronger than 11 dBZ. Meanwhile, KuPR measures the intensity of relatively heavy precipitation, whereas CPR does not, due to the saturation of attenuation signals. Precipitation measurements made using KuPR revealed that radar reflectivity, or the intensity of precipitation, generally increases downward, and this feature is especially clear over the coastal ocean and lowlands around the south coast of Alaska.

(2) Over the ocean, it was found that most precipitation falls on the surface as rainfall and mixed-phase precipitation, which can be captured by KuPR. KuPR statistics showed that both the frequency and intensity of precipitation increase approaching the coastline over the ocean. The sorting of precipitation events according to the CPR cloud scenario classification and DPR rainfall type classification revealed that precipitation events in this region are mostly brought by nimbostratus clouds, which are related to frontal cloud systems associated with extratropical cyclones. These results indicate that owing to the strong convergence of moisture at a low-level due to orographic effects, relatively heavy precipitation from nimbostratus clouds frequently occurs above coastal waters.

(3) Over the coastal mountains, while the frequency of mixed-phase precipitation is low, the frequency of snow is especially high, which is rarely observed by KuPR. Though the heavy snowfall events (CPR reflectivity > 11 dBZ) rarely occur, the snowfall amount brought by the events accounts for nearly half of the total snowfall amount detected by CPR, suggesting infrequent heavy snowfall events make non-negligible contribution to the precipitation climatology in Alaska. Snowfall in coastal mountains is mainly brought by nimbostratus clouds, which are initially produced or enhanced along the coastline and then advected inland as they are swept along by the strong cross-barrier component of winds in the middle troposphere. In contrast, shallow cumuliform clouds are frequently detected over the coastal mountains under the conditions of weak cross-barrier winds. Snowfall from this type of cloud is not heavy, and it is thus well detected by the CPR but rarely detected by KuPR.

(4) The seasonal analysis of KuPR revealed that precipitation is most frequently brought in SON when extratropical cyclones more frequently exist in the Gulf of Alaska, whereas diurnal analysis showed that the KuPR precipitation frequency is a maximum over the coastal water with small diurnal variability during SON, DJF, and MAM periods, suggesting moisture flows associated with extratropical cyclones are an important factor of precipitation in this region. During JJA, there are two peaks of precipitation frequency with some diurnal variation: an inland peak having its maximum in the afternoon (12:00–18:00 LST) and a peak on coastal water having its maximum in the early morning (0:00–6:00 LST). However, the amplitude of diurnal variation is small relative to total precipitation especially over the ocean, and the maximum precipitation peak appears on coastal water at any time. This distribution of precipitation with small diurnal variations around the coast of Alaska is different from that with strong diurnal variation in such regions as the Indonesian Maritime Continent and northwestern South America in the tropics, suggesting the dominance of synoptic-scale water vapor transport from the ocean even in summer. Case studies showed that frontal systems and moisture flows associated with extratropical cyclones that arrive from the Gulf of Alaska are blocked by terrain and delayed around the coast. This leads to long-lasting precipitation along the coastline.

This study clarified the climatological picture of precipitation with large gradients of precipitation characteristics around the south coast of Alaska, which was poorly observed before multiple spaceborne radars became available. However, observations by spaceborne radars face the problem that precipitation particles cannot be observed in the lower 1 km owing to ground clutter obstruction (Battaglia et al. 2020). This study also showed that the intensity and frequency of precipitation increase toward the lower layers of the troposphere, and some precipitating particles that actually fell on the ground surface may differ from

those obtained by spaceborne radars. Further research on changes in precipitation particles and orographic effects on air flow in the lowest 1 km is needed to clarify overall features of precipitation in mountainous areas at higher latitudes.

Acknowledgment

This study was supported by the JAXA Precipitation Measuring Mission (PMM) project and JSPS KAKENHI Grant 19H01969. This work was also conducted as a joint research program of CEReS, Chiba University (2019). The authors are very grateful to two anonymous reviewers for their constructive and helpful comments.

Supplements

Three supplemental materials compare the vertical profile of radar products and that of the physical quantity from ERA5 reanalysis for a KuPR case in Fig. 10e and a CPR case in Fig. 10f. Figure S1 shows vertical profiles of the (a) KuPR radar reflectivity, (b) KuPR precipitation rate for a section of orbit 4513 on 14 December 2014, (c) coincident ECMWF ERA5 cloud fraction, and (d) the cloud water content at 18:00 UTC. Figure S2 shows vertical profiles of (a) the CloudSat CPR radar reflectivity, (b) the CPR cloud classification for a section of orbit 45914 on 14 December 2014, (c) the coincident ECMWF ERA5 cloud fraction, and (d) the cloud water content at 23:00 UTC. Figure S1 is the vertical cross section of the KuPR nadir track shown in Fig. S3a, whereas Figure S2 is the vertical cross section of the CPR track shown in Fig. S3b.

References

Awaka, J., M. Le, V. Chandrasekar, N. Yoshida, T. Higashiuwatoko, T. Kubota, and T. Iguchi, 2016: Rain type classification algorithm module for GPM dual-frequency precipitation radar. *J. Atmos. Oceanic Technol.*, **33**, 1887–1898.

Battaglia, A., P. Kollias, R. Dhillon, R. Roy, S. Tanelli, K. Lamer, M. Grecu, M. Lebsock, D. Watters, K. Mroz, G. Heymsfield, L. Li, and K. Furukawa, 2020: Spaceborne cloud and precipitation radars: Status, challenges, and ways forward. *Rev. Geophys.*, **58**, e2019RG000686, doi:10.1029/2019RG000686.

Berg, W., T. L'ecuyer, and J. M. Haynes, 2010: The distribution of rainfall over oceans from spaceborne radars. *J. Appl. Meteor. Climatol.*, **49**, 535–543.

Biasutti, M., S. E. Yuter, C. D. Burleyson, and A. H. Sobel, 2012: Very high resolution rainfall patterns measured by TRMM precipitation radar: Seasonal and diurnal cycles. *Climate Dyn.*, **39**, 239–258.

Casella, D., G. Panegrossi, P. Sanò, A. C. Marra, S. Dietrich, B. T. Johnson, and M. S. Kulie, 2017: Evaluation of the GPM-DPR snowfall detection capability: Comparison with CloudSat-CPR. *Atmos. Res.*, **197**, 64–75.

Chen, S., Y. Hong, M. Kulie, A. Behrangi, P. M. Stepanian, Q. Cao, Y. You, J. Zhang, J. Hu, and X. Zhang, 2016: Comparison of snowfall estimates from the NASA CloudSat cloud profiling radar and NOAA/NSSL multi-radar multi-sensor system. *J. Hydrol.*, **541**, 862–872.

Colle, B. A., K. A. Loescher, G. S. Young, and N. S. Winstead, 2006: Climatology of barrier jets along the Alaskan coast. Part II: Large-scale and sounding composites. *Mon. Wea. Rev.*, **134**, 454–477.

Haynes, J. M., T. S. L'Ecuyer, D. Vane, G. L. Stephens, and D. Reinke, 2013: Level 2-C precipitation column algorithm product process description and interface control document. Version P2_R04. *CloudSat Project, A NASA Earth System Science Pathfinder Mission*, 17 pp. [Available at http://www.cloudsat.cira.colostate.edu/sites/default/files/products/files/2C-PRECIP-COLUMN_PDICD.P2_R04.20130124.pdf.]

Hersbach, H., and D. Dee, 2016: ERA5 reanalysis is in production. *ECMWF Newsletter*, No.147. [Available at https://www.ecmwf.int/en/newsletter/147/news/era5-reanalysis-production.]

Hirose, M., S. Shimizu, R. Oki, T. Iguchi, D. A. Short, and K. Nakamura, 2012: Incidence-angle dependency of TRMM PR rain estimates. *J. Atmos. Oceanic Technol.*, **29**, 192–206.

Hirose, M., Y. N. Takayabu, A. Hamada, S. Shige, and M. K. Yamamoto, 2017: Spatial contrast of geographically induced rainfall observed by TRMM PR. *J. Climate*, **30**, 4165–4184.

Hou, A. Y., R. K. Kakar, S. Neeck, A. A. Azarbarzin, C. D. Kummerow, M. Kojima, R. Oki, K. Nakamura, and T. Iguchi, 2014: The Global Precipitation Measurement mission. *Bull. Amer. Meteor. Soc.*, **95**, 701–722.

Houze, R. A., Jr., 2012: Orographic effects on precipitating clouds. *Rev. Geophys.*, **50**, RG1001, doi:10.1029/2011RG000365.

Houze, R. A., Jr., L. A. McMurdie, W. A. Petersen, M. R. Schwaller, W. Baccus, J. D. Lundquist, C. F. Mass, B. Nijssen, S. A. Rutledge, D. R. Hudak, S. Tanelli, G. G. Mace, M. R. Poellot, D. P. Lettenmaier, J. P. Zagrodnik, A. K. Rowe, J. C. DeHart, L. E. Madaus, H. C. Barnes, and V. Chandrasekar, 2017: The Olympic Mountains Experiment (OLYMPEX). *Bull. Amer. Meteor. Soc.*, **98**, 2167–2188.

Iguchi, T., 2020: Dual-frequency Precipitation Radar (DPR) on the Global Precipitation Measurement (GPM) mission's core observatory. *Satellite Precipitation Measurement. Vol.1*. Levizzani, V., C. Kidd., D. B. Kirschbaum, C. D. Kummerow, K. Nakamura, and F. J. Turk (eds.), Advances in Global Change Research, No.67, Springer, 183–192.

Iguchi, T., S. Seto, R. Meneghini, N. Yoshida, J. Awaka, M. Le, V. Chandrasekar, S. Brodzik, and T. Kubota, 2018: *GPM/DPR Level-2 Algorithm Theoretical Basis Document*. NASA Global Precipitation Measurement, 127 pp. [Available at https://www.eorc.jaxa.jp/GPM/doc/algorithm/ATBD_DPR_201811_with_Appendix3b.pdf.]

Kikuchi, K., and B. Wang, 2008: Diurnal precipitation regimes in the global tropics. *J. Climate*, **21**, 2680–2696.

Kojima, M., T. Miura, K. Furukawa, Y. Hyakusoku, T. Ishikiri, H. Kai, T. Iguchi, H. Hanado, and K. Nakagawa, 2012: Dual-frequency precipitation radar (DPR) development on the Global Precipitation Measurement (GPM) core observatory. *Proc. SPIE*, **8528**, 85281A, doi:10.1117/12.976823.

Kozu, T., T. Kawanishi, H. Kuroiwa, M. Kojima, K. Oikawa, H. Kumagai, K. Okamoto, M. Okumura, H. Nakatsuka, and K. Nishikawa, 2001: Development of precipitation radar onboard the Tropical Rainfall Measuring Mission (TRMM) satellite. *IEEE Trans. Geosci. Remote Sens.*, **39**, 102–116.

Kubota, T., T. Iguchi, M. Kojima, L. Liao, T. Masaki, H. Hanado, R. Meneghini, and R. Oki, 2016: A statistical method for reducing sidelobe clutter for the Ku-band precipitation radar onboard the GPM Core Observatory. *J. Atmos. Oceanic Technol.*, **33**, 1413–1428.

Kulie, M. S., L. Milani, N. B. Wood, S. A. Tushaus, R. Bennartz, and T. S. L'Ecuyer, 2016: A shallow cumuliform snowfall census using spaceborne radar. *J. Hydrometeor.*, **17**, 1261–1279.

Kummerow, C., W. Barnes, T. Kozu, J. Shiue, and J. Simpson, 1998: The Tropical Rainfall Measuring Mission (TRMM) sensor package. *J. Atmos. Oceanic Technol.*, **15**, 809–817.

Mapes, B. E., T. T. Warner, M. Xu, and A. J. Negri, 2003a: Diurnal patterns of rainfall in northwestern South America. Part I: Observations and context. *Mon. Wea. Rev.*, **131**, 799–812.

Mapes, B. E., T. T. Warner, and M. Xu, 2003b: Diurnal patterns of rainfall in northwestern South America. Part III: Diurnal gravity waves and nocturnal convection offshore. *Mon. Wea. Rev.*, **131**, 830–844.

Marchand, R., G. G. Mace, T. Ackerman, and G. Stephens, 2008: Hydrometeor detection using Cloudsat—An earth-orbiting 94-GHz cloud radar. *J. Atmos. Oceanic Technol.*, **25**, 519–533.

Medina, S., E. Sukovich, and R. A. Houze, Jr., 2007: Vertical structures of precipitation in cyclones crossing the Oregon Cascades. *Mon. Wea. Rev.*, **135**, 3565–3586.

Mesquita, M. S., D. E. Atkinson, and K. I. Hodges, 2010: Characteristics and variability of storm tracks in the North Pacific, Bering Sea, and Alaska. *J. Climate*, **23**, 294–311.

Mori, S., J. Hamada, Y. I. Tauhid, M. D. Yamanaka, N. Okamoto, F. Murata, N. Sakurai, H. Hashiguchi, and T. Sribimawati, 2004: Diurnal land–sea rainfall peak migration over Sumatera island, Indonesian maritime continent, observed by TRMM satellite and intensive rawinsonde soundings. *Mon. Wea. Rev.*, **132**, 2021–2039.

Neiman, P. J., F. M. Ralph, G. A. Wick, J. D. Lundquist, and M. D. Dettinger, 2008: Meteorological characteristics and overland precipitation impacts of atmospheric rivers affecting the West Coast of North America based on eight years of SSM/I satellite observations. *J. Hydrometeor.*, **9**, 22–47.

Nesbitt, S. W., and A. M. Anders, 2009: Very high resolution precipitation climatologies from the Tropical Rainfall Measuring Mission precipitation radar. *Geophys. Res. Lett.*, **36**, L15815, doi:10.1029/2009GL038026.

Ogino, S.-Y., M. D. Yamanaka, S. Mori, and J. Matsumoto, 2016: How much is the precipitation amount over the tropical coastal region? *J. Climate*, **29**, 1231–1236.

Ogino, S.-Y., M. D. Yamanaka, S. Mori, and J. Matsumoto, 2017: Tropical coastal dehydrator in global atmospheric water circulation. *Geophys. Res. Lett.*, **44**, 11636–11643.

Olson, J. B., and B. A. Colle, 2009: Three-dimensional idealized simulations of barrier jets along the southeast coast of Alaska. *Mon. Wea. Rev.*, **137**, 391–413.

Overland, J. E., and N. Bond, 1993: The Influence of coastal orography: The Yakutat Storm. *Mon. Wea. Rev.*, **121**, 1388–1397.

Shige, S., and C. D. Kummerow, 2016: Precipitation-top heights of heavy orographic rainfall in the Asian monsoon region. *J. Atmos. Sci.*, **73**, 3009–3024.

Shige, S., Y. Nakano, and M. K. Yamamoto, 2017: Role of orography, diurnal cycle, and intraseasonal oscillation in summer monsoon rainfall over the western Ghats and Myanmar coast. *J. Climate*, **30**, 9365–9381.

Skofronick-Jackson, G., M. Kulie, L. Milani, S. J. Munchak, N. B. Wood, and V. Levizzani, 2019: Satellite estimation of falling snow: A Global Precipitation Measurement (GPM) Core Observatory perspective. *J. Appl. Meteorol. Climatol.*, **58**, 1429–1448.

Stephens, G. L., D. G. Vane, R. J. Boain, G. G. Mace, K. Sassen, Z. Wang, A. J. Illingworth, E. J. O'connor, W. B. Rossow, S. L. Durden, S. D. Miller, R. T. Austin, A. Benedetti, C. Mitrescu, and the CloudSat Science Team, 2002: The CloudSat mission and the A-Train. *Bull. Amer. Meteor. Soc.*, **83**, 1771–1790.

Tanelli, S., S. L. Durden, E. Im, K. S. Pak, D. G. Reinke, P. Partain, J. M. Haynes, and R. T. Marchand, 2008: CloudSat's cloud profiling radar after two years in orbit: Performance, calibration, and processing. *IEEE Trans. Geosci. Remote Sens.*, **46**, 3560–3573.

Tang, G., Y. Wen, J. Gao, D. Long, Y. Ma, W. Wan, and Y. Hong, 2017: Similarities and differences between three coexisting spaceborne radars in global rainfall and snowfall estimation. *Water Resour. Res.*, **53**, 3835–3853.

Toyoshima, K., H. Masunaga, and F. A. Furuzawa, 2015: Early evaluation of Ku- and Ka-band sensitivities for the Global Precipitation Measurement (GPM) Dual-frequency Precipitation Radar (DPR). *SOLA*, **11**, 14–17.

Wang, Z., and K. Sassen, 2007: Level 2 cloud scenario classification product process description and interface control document. Version 5.0. *CloudSat Project, A NASA Earth System Science Pathfinder Mission*, 50 pp. [Available at http://www.cloudsat.cira.colostate.edu/sites/default/files/products/files/2B-CLDCLASS_PDICD.P_R04.20070724.pdf.]

Wood, N. B., T. S. L'Ecuyer, D. Vane, G. L. Stephens, and P. Partain, 2013: Level 2C snow profile process description and interface control document. *CloudSat Project, A NASA Earth System Science Pathfinder Mission*, 21 pp. [Available at http://www.cloudsat.cira.colostate.edu/sites/default/files/products/files/2C-SNOW-PROFILE_PDICD.P_R04.20130210.pdf.]

Yamanaka, M. D., 2016: Physical climatology of Indonesian maritime continent: An outline to comprehend observational studies. *Atmos. Res.*, **178–179**, 231–259.

Yang, S., and E. A. Smith, 2006: Mechanisms for diurnal variability of global tropical rainfall observed from TRMM. *J. Climate*, **19**, 5190–5226.

Yuter, S. E., and R. A. Houze, Jr., 1995: Three-dimensional kinematic and microphysical evolution of Florida Cumulonimbus. Part II: Frequency distributions of vertical velocity, reflectivity, and differential reflectivity. *Mon. Wea. Rev.*, **123**, 1941–1963.

Zagrodnik, J. P., L. A. McMurdie, and R. A. Houze, Jr., 2018: Stratiform precipitation processes in cyclones passing over a coastal mountain range. *J. Atmos. Sci.*, **75**, 983–1004.

Zagrodnik, J. P., L. A. McMurdie, R. A. Houze, Jr., and S. Tanelli, 2019: Vertical structure and microphysical characteristics of frontal systems passing over a three-dimensional coastal mountain range. *J. Atmos. Sci.*, **76**, 1521–1546.